

# Radio propagation measurement and cluster-based analysis for millimeter-wave cellular systems in dense urban environments\*

Peize ZHANG<sup>1,2</sup>, Haiming WANG<sup>1,2</sup>, Wei HONG<sup>1,2</sup>

<sup>1</sup>State Key Laboratory of Millimeter Waves, Southeast University, Nanjing 210096, China

<sup>2</sup>Purple Mountain Laboratories, Nanjing 211111, China

E-mail: pzzhang@seu.edu.cn; hmwang@seu.edu.cn; weihong@seu.edu.cn

Received Sept. 23, 2020; Revision accepted Jan. 6, 2021; Crosschecked Mar. 3, 2021

**Abstract:** The deployment of millimeter-wave (mmWave) cellular systems in dense urban environments with an acceptable coverage and cost-efficient transmission scheme is essential for the rollout of fifth-generation and beyond technology. In this paper, cluster-based analysis of mmWave channel characteristics in two typical dense urban environments is performed. First, radio propagation measurement campaigns are conducted in two identified mmWave bands of 28 and 39 GHz in a central business district and a dense residential area. The custom-designed channel sounder supports high-efficiency directional scanning sounding, which helps collect sufficient data for statistical channel modeling. Next, using an improved auto-clustering algorithm, multipath clusters and their scattering sources are identified. An appropriate measure for inter- and intra-cluster characteristics is provided, which includes the cluster number, the Ricean  $K$ -factor, root-mean-squared (RMS) delay spread, RMS angular spread, and their correlations. Comparisons of these parameters across two mmWave bands for both line-of-sight (LoS) and non-line-of-sight (NLoS) links are given. To shed light on the blockage effects, detailed analysis of the propagation mechanisms corresponding to each NLoS cluster is provided, including reflection from exterior walls and diffraction over building corners and rooftops. Finally, the results show that the cluster-based analysis takes full advantage of mmWave beamspace channel characteristics and has further implications for the design and deployment of mmWave wireless networks.

**Key words:** Millimeter-wave communication; Clustering; Diffraction; Multipath channels; Propagation measurement

<https://doi.org/10.1631/FITEE.2000489>

**CLC number:** TN929.5

## 1 Introduction

To meet the requirements of multi-gigabit-per-second data rate and millisecond-level end-to-end latency for fifth-generation (5G) and beyond

(B5G) mobile communication systems, millimeter-wave (mmWave) communication has emerged as a prior technology rollout solution (Rappaport et al., 2013; Saad et al., 2020; You et al., 2021). In 2019, the spectra in the 24.25–27.5, 37–43.5, 45.5–47, 47.2–48.2, and 66–71 GHz bands were identified at the World Radiocommunication Conference 2019, which further promoted the development of mmWave communication for 5G/B5G (ITU, 2019). However, the implementation of mmWave cellular networks in outdoor environments is much more challenging with

† Corresponding author

\* Project supported in part by the National Key R&D Program of China (No. 2020YFB1804901), the National Natural Science Foundation of China (No. 61960206006), the Key R&D Program of Jiangsu Province of China (No. BE2018121), and the China Scholarship Council (CSC) Program

ORCID: Peize ZHANG, <https://orcid.org/0000-0002-2944-5973>; Haiming WANG, <https://orcid.org/0000-0002-6156-258X>

© Zhejiang University Press 2021

respect to transmission schemes and performance, network architectures, and system deployments (Yuan et al., 2020; You et al., 2021).

With the increase in carrier frequency, a distinguishing feature of outdoor cellular systems is the decrease of cell radii because of the large propagation attenuation and severe vulnerability to blockages. To achieve higher outdoor coverage probability and enhance the connectivity, base station (BS) cooperation in mmWave ultra-dense networks is of great importance (Xiao et al., 2017). In addition, a heterogeneous network integrating microwave macro BSs and mmWave small-cell BSs is recognized to be a promising technology for future mmWave communications (Saad et al., 2020). The complicated network architectures indicate that traditional cellular networks with BSs on a grid are highly idealized and intractable for mmWave systems, which involve challenges with respect to deployment cost, power consumption, and coverage (Andrews et al., 2017). Hence, there has been great interest in theoretically and experimentally analyzing the coverage and data rate of mmWave cellular networks from the perspective of channel characteristics (Bai et al., 2014; Yu et al., 2017). Another distinct feature of mmWave cellular communication is directional transmission. The sparse nature of mmWave propagation environments indicates that cluster-based representation of mmWave channels is appropriate, where the subpaths within each cluster share similar propagation delays, angle of arrival, and angle of departure (Hur et al., 2016; Ko et al., 2017). As a consequence, directional beams can be used to sweep through all possible directions and track effective clusters based on hybrid digital and analog beamforming (Roh et al., 2014; Sohrabi and Yu, 2016).

Extensive mmWave channel measurement campaigns have been conducted in various urban environments, such as university campuses at 38, 60, and 73 GHz (Rappaport et al., 2015), densely built-up downtowns at 28 and 60 GHz (Ko et al., 2017; Raghavan et al., 2017), and street canyons at 28, 38, and 60 GHz (Haneda et al., 2016; Hur et al., 2016). The measurements show that an optimistic assessment of outdoor mmWave cellular systems can be performed with cell radii up to the order of 200 m. Basically, highly directional horn antennas have been leveraged to increase the dynamic range of channel sounders and synthesize narrow beams for omnidi-

rectional channel modeling via antenna steering in both azimuth and elevation directions mechanically. Apart from the investigation on large-scale path-loss models, there is a dearth of elaborate analysis on space-time channel characteristics down to the cluster level in existing studies. Moreover, only signals from one or two fixed zenith angles of arrival/zenith angles of departure (ZoA/ZoD) have been measured due to the fact that traditional mmWave channel sounders using the directional scanning sounding (DSS) method are time-consuming to collect sufficient channel data. It is also important to note that some mmWave small-scale channel model parameters are frequency-dependent and environment-specific (3GPP, 2018; Zhang et al., 2018), but only a handful of outdoor measurement activities focus on these effects with the same measurement configurations (Rappaport et al., 2012; Raghavan et al., 2017).

Previous experimental investigations indicate that a large fraction of the signal energy is concentrated on the direct path in line-of-sight (LoS) scenarios, and that specular reflection from the exterior walls of buildings plays a role in non-line-of-sight (NLoS) scenarios (Hur et al., 2016; Ko et al., 2017). These observations are also in line with the previously reported results (Zhao et al., 2013), where outdoor building materials are excellent reflectors with large reflection coefficients, but ground reflection is negligible (Rappaport and Deng, 2015). The analysis of diffraction loss over rooftop and building corners has been provided in Kim et al. (2017) and Rappaport et al. (2017) based on both the knife-edge diffraction (KED) model and the creeping wave linear model; these models were derived as a function of the diffraction angle. However, little is known about the implications of these outdoor mmWave propagation mechanisms on system design with extending coverage.

In this study, we remedy these gaps based on a comprehensive measurement campaign conducted in two typical urban macrocell (UMa) scenarios at 28 and 39 GHz using our custom-designed high-efficiency channel sounder (Li J et al., 2019). The contributions are listed as follows:

1. Details of cellular-type channel measurement campaigns performed in urban central business district (CBD) and dense residential area (DRA) environments for both LoS and NLoS links in the two

identified mmWave bands are presented. Thousands of effective directional power delay profiles (PDPs) are collected for statistical channel modeling.

2. An improved auto-clustering algorithm is developed, including initial cluster centroid selection, two-step KPowerMeans clustering, outlier detection and pruning, and cluster validation, taking account of the sparse structure of mmWave channels in delay and angular domains. Its advantages in such aspects as clustering accuracy and efficiency could distinguish temporally sparse clusters with a lower number of iterations.

3. The cluster-level parameters are estimated, including the Ricean  $K$ -factor, number of clusters, delay spread (DS), azimuth angular spread of arrival (ASA), and zenith angular spread of arrival (ZSA). The statistics of these channel parameters across multiple bands and scenarios are extracted, as well as their correlations. Modeling results not only complete the present 3GPP channel models above 6 GHz (3GPP, 2018), but also have further implications on physical layer design.

4. The mapping results reveal the consistency between multipath clusters and physical scatterers in the surrounding environments, where the impact of different propagation mechanisms on the birth of clusters is investigated in several specific scenarios.

## 2 Cellular-type channel measurements

### 2.1 Channel sounder hardware and setup

A brief description of the custom-designed mmWave channel sounder using commercial off-the-shelf (COTS) instruments is given here; details can be found in our previous paper (Li J et al., 2019). Fig. 1 depicts the schematic of the channel measurement system. At the transmitter (TX) side, a high-performance vector signal generator (VSG) is used to continuously transmit a binary periodic complementary Golay pair of length 4096 stated at the clock rate of 300 MHz. The signals of radio frequency (RF) null-to-null bandwidth of 600 MHz at the center frequencies of 28 and 39 GHz, corresponding to the delay resolution of 3.3 ns, are emitted via a wideband wide-beam horn antenna fixed on a tripod. Compared with the widely used pseudonoise (PN) sequence, this Golay pair exhibits perfect complementary auto-correlation properties (Wang et al.,

2007). At the receiver (RX) side, a vector signal analyzer (VSA) is used for raw data acquisition. The narrow-beam horn antennas are placed on a custom-designed positioner to scan in the azimuth and elevation directions automatically, enabling the capturing of spatial multipath signals. Both the transceiver antennas are vertically polarized. In addition, power amplifiers (PAs) and low-noise amplifiers (LNAs) for each concerned band are used to extend the system's dynamic range.

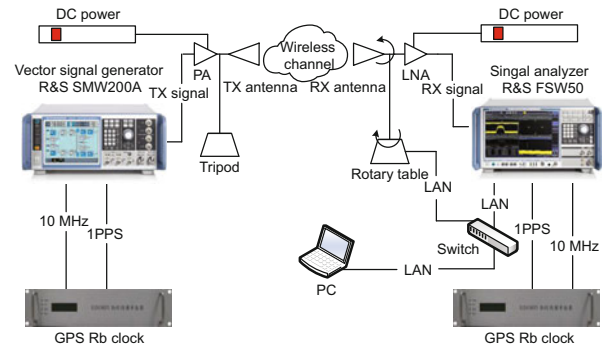


**Fig. 1 Commercial off-the-shelf (COTS) instruments based mmWave channel measurement setup description in dense urban environments**

Table 1 shows the measurement settings for the sounder at 28 and 39 GHz. Note that the specifications for TX and RX antennas, such as half-power beamwidth (HPBW) and antenna gain, are obtained based on the measurement results. The over-the-air reference measurements are conducted with TX and RX antennas aligned and separated by 5 m. Then we continuously reduce the transmitted power until there is no detectable signal beyond the noise floor plus a margin of 8 dB. Generally, the signal-to-noise ratio (SNR) threshold is selected depending on the performance of the sounder. For example, a margin of 10 dB above the noise floor was used in Duplich et al. (2019). In this study, an 8-dB SNR threshold is chosen including 3-dB margin relative to the widely used 5-dB threshold (Rappaport et al., 2015). The 5-dB SNR threshold corresponds to using the rule of standard deviation where 99.7% of the values are within three times of the standard deviation. Consequently, under such measurement configurations, the overall measurable path loss of the sounder, i.e., 154 and 159 dB at 28 and 39 GHz, respectively, is high enough to ensure that the received signals over all RX locations are valid to obtain effective subpaths for statistical channel modeling (Rappaport et al.,

2015). As for computing the dynamic range of the sounder (i.e., the RX) (Bas et al., 2019), the estimated received power is beyond the RX sensitivity when the input power to the RX RF connector is  $-71/-73$  dBm at 28/39 GHz. The field measured 1-dB compression input power for the two LNAs is  $-16/-21$  dBm at 28/39 GHz, so the dynamic ranges of the sounder are 55 and 52 dB at these two bands, respectively.

**Table 1 Specifications of the multi-frequency channel sounder**

Parameter	Value	
Carrier frequency (GHz)	28	39
Clock rate of the sequence (MHz)	300	
RF null-to-null bandwidth (MHz)	600	
Delay resolution (ns)	3.3	
TX antenna HPBW ( $^{\circ}$ )	60	50
TX antenna gain (dB)	11.4	18.7
PA gain (dB)	20	18
PA P1dB (dBm)	30	28
RX antenna HPBW ( $^{\circ}$ )	8.8	8.1
RX antenna gain (dB)	25.6	27.7
LNA gain (dB)	33	35
Polarization	Vertical-vertical	

RF: radio frequency; TX: transmitter; HPBW: half-power beamwidth; PA: power amplifier; LNA: low-noise amplifier

Since the sounder is specialized for outdoor long-distance channel measurements, the traditional synchronization method using coaxial cables to connect TX and RX is infeasible (Zhang et al., 2018). Here, two separate GPS Rubidium (Rb) standard references are connected to the VSG and the VSA, respectively, for frequency synchronization with stable 10 MHz outputs and data reception with periodical 1 pulse-per-second (1PPS) trigger signals. Thanks to the employment of Rb standard references, absolute propagation delay can be obtained following the calibration method developed (MacCartney and Rappaport, 2017). However, only relative propagation delay was considered in their work due to the measurement limitations in actual outdoor environments. During the measurements, an uninterruptible power supply (UPS) unit was used at the RX cart with up to 4 h of battery power.

Back-to-back calibrations are performed before the measurements via directly connecting the transceiver RF front ends, in which the PA at the transmitter and the LNA at the receiver are included. Fig. 2 shows the normalized PDP for the thru connection in the back-to-back tests at 28 and

39 GHz with the transmitted power of  $-65$  dBm. During the calibration measurements, the sounding sequence is transmitted 10 times on average at the two considered bands. Thanks to using the COTS instruments, it shows better temporal stability of calibrations. Note that the normalized noise floor at 28 GHz is 4.1 dB lower than that at 39 GHz. The captured system impulse responses ensure a precise PDP estimation after deembedding the impact of channel sounder, and can be used to calibrate the insertion loss and transmission delay of the COTS-based sounder. Here, the threshold of 8 dB above the noise floor is employed, resulting in 37.9 and 33.3 dB system gains at 28 and 39 GHz, respectively.

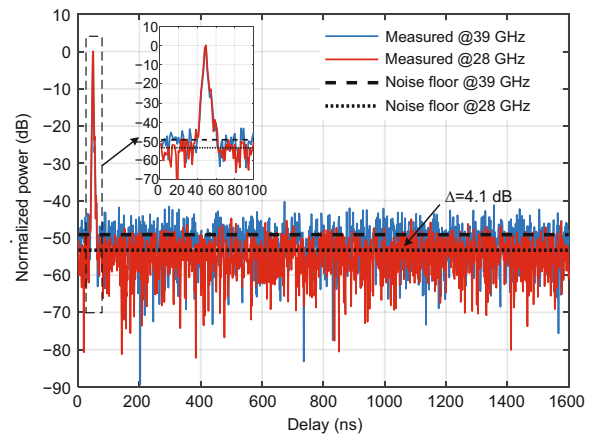


**Fig. 2 Normalized power delay profiles (PDPs) for the system responses at 28 and 39 GHz obtained via back-to-back measurements with transmitted power of  $-65$  dBm, including the impact of the power amplifier (PA) at the transmitter and the low-noise amplifier (LNA) at the receiver**

## 2.2 Measurement environments and procedures

As shown in Fig. 3, outdoor macrocell channel measurements were conducted at both 28 and 39 GHz in the downtown of Nanjing, China, which provides two typical rich multipath urban environments. Note that the measurement campaigns in two dense urban environments were both conducted from 11 pm to 5 am, such that channels were generally static during the measurements. The first set of UMa measurements was obtained in the CBD environment as shown in Fig. 3a, where the surrounding buildings were coated with metal billboards or light-emitting diode (LED) screens. The CBD-TX was located on the rooftop of the Hanting Hotel

(14-story high, 45 m above ground level). Overall, 46 RX locations were chosen, including 25 locations in the LoS scenario served by two sectors and 21 locations in the NLoS scenario served only by sector 2. The TX-RX separation distances were between 56 and 202 m. The second set of UMa measurements was obtained in the DRA environment as shown in Fig. 3b. The distinguishing feature of this environment is the presence of concrete walls on the building exteriors, leading to poor reflections compared with the CBD environment. Measurement data were collected with the DRA-TX located on the rooftop of Sumao Building at a height of 50 m above ground, while the RX was at 1.9 m and moved to 36 locations with TX-RX link distances ranging from 55 to 280 m. Among all the 36 RX locations, 13 LoS locations and 23 NLoS locations were taken into consideration. Note that the NLoS links in DRA represent that no clear direct path exists due to the blockage by large tree trunks (e.g., RX 12–15) or buildings (e.g., RX 17–21 and 25–36), whereas in CBD, all NLoS RXs were blocked by the surrounding buildings. For convenience, Table 2 provides the TX-RX location combinations and their corresponding sectors in operation.

The PDP measurements in the two dense urban environments were taken using a fixed TX antenna

downtilt of  $105^\circ$  for sector coverage with two specific TX azimuth angles ( $-20^\circ$  and  $+40^\circ$ ). Then, five different RX elevations of  $-70^\circ$ ,  $-80^\circ$ ,  $90^\circ$ ,  $+100^\circ$ , and  $+110^\circ$  were used, and the whole  $360^\circ$  azimuthal scans of the RX antennas were conducted in increments of  $10^\circ$ .

### 3 Cluster-based channel characterization

#### 3.1 Clustering multipath components

Effective multipath components (MPCs) and their characterization, including power  $p$ , delay  $\tau$ , azimuth angle of arrival (AoA)  $\phi$ , and ZoA  $\theta$ , are the basic inputs for the clustering algorithm. MPCs can

**Table 2 TX-RX location combinations and their serving sectors**

Environment	Sector (azimuth)	Scenario	RX position
CBD	Sector 1 ( $-20^\circ$ )	LoS	1–18
	Sector 2 ( $+40^\circ$ )	LoS	12–25
		NLoS	25–46
DRA	Sector 1 ( $-20^\circ$ )	LoS	4–11, 16, 22–24
		NLoS	1–3, 12–15, 17–21
	Sector 2 ( $+40^\circ$ )	LoS	22–24
		NLoS	25–36

TX: transmitter; RX: receiver; CBD: central business district; DRA: dense residential area; LoS: line-of-sight; NLoS: non-light-of-sight

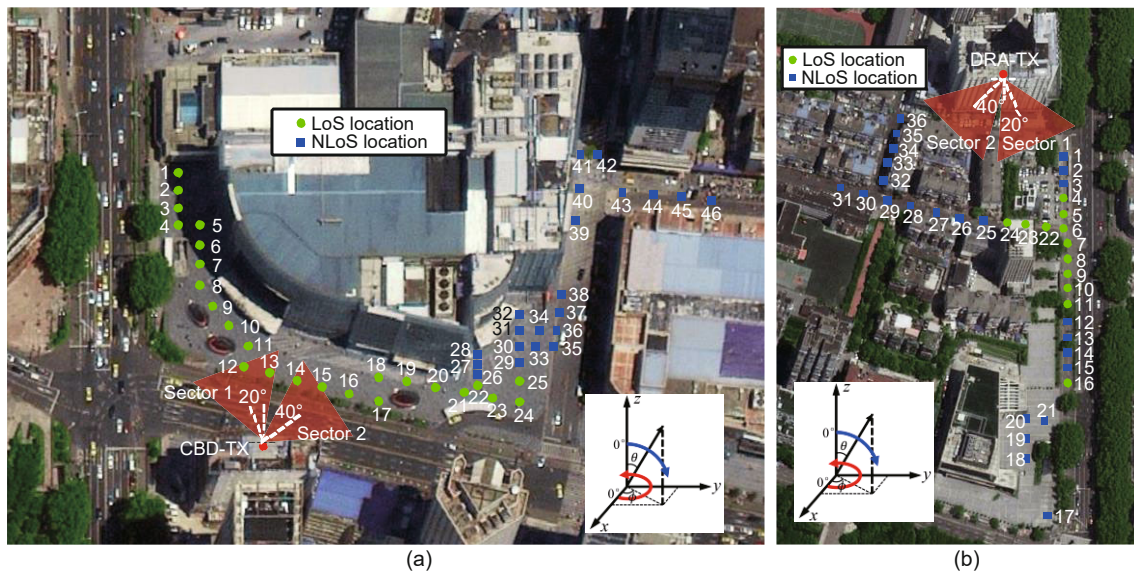


**Fig. 3 TX and RX locations in CBD (a) and DRA (b) environments**

Red dots: TX locations on the rooftop of buildings; green dots: RX locations in the line-of-sight (LoS) scenario; blue squares: RX locations in the non-light-of-sight (NLoS) scenario. References to color refer to the online version of this figure

be extracted from directional PDP using the peak detection algorithm. If the peak power is larger than the detection level  $P_D$ , this peak will be selected as an effective MPC.  $P_D$  (in dB) is defined as follows:

$$P_D = \max \{P_{\max} - P_{\text{th}}, N_o + \gamma\}, \quad (1)$$

where  $P_{\text{th}}$  is the power threshold relative to the maximum received peak power  $P_{\max}$ ,  $N_o$  is the noise floor calculated by the variance of last hundred nanoseconds of each channel impulse response (CIR), and  $\gamma$  is the SNR. The maximum received peak power  $P_{\max}$  is computed as

$$P_{\max} = \max_{1 \leq i \leq 180} p_{\max,i}, \quad (2)$$

where  $p_{\max,i}$  denotes the peak power for the  $i^{\text{th}}$  directional PDP, and there are totally 180 directional PDPs (36 in the azimuth plane and 5 in the elevation plane) at each TX-RX pair. Both  $P_{\text{th}}$  and SNR are empirical values depending on the carrier frequency, bandwidth, and environments, and in general, contain the typical value of 3 dB as safety margin.

Fig. 4 shows a typical measured directional PDP for the NLoS scenario in CBD environments, where the effective PDP filtering the contribution of noise floor (red part) is estimated following our previously proposed method (Wang et al., 2019). The 30-dB power threshold and 20-dB SNR are employed to compute  $P_D$ . Two time clusters with different time

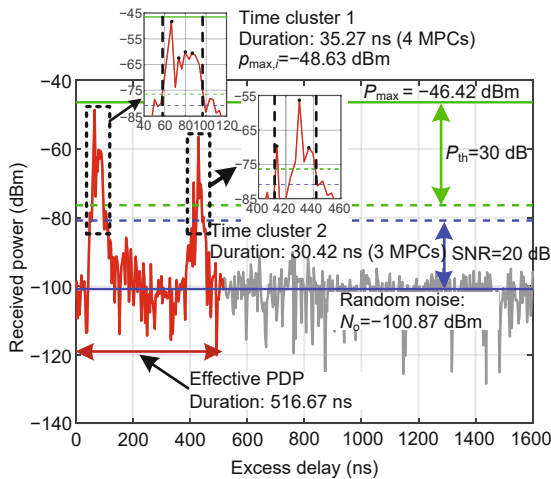


**Fig. 4** Illustration of the peak detection algorithm to extract effective multipath components (MPCs) based on the typical measured directional power delay profile (PDP) at 28 GHz for CBD-RX 38 with  $\theta = 340^\circ$  and  $\phi = 80^\circ$ , where two time clusters and a total of seven MPCs are estimated (References to color refer to the online version of this figure)

durations have been identified using the similar representation by Samimi and Rappaport (2016). Sequentially, a total of seven effective MPCs (the black marks shown by the insets), whose received power levels are above  $-76.42$  dBm (the green dotted line), are detected directly from the measured data points using the peak detection algorithm. These effective MPCs share the same AoA and ZoA identified during the measurements but have various propagation delays which concentrate mainly in two time clusters with an approximate difference of 363.33 ns. Note that the larger  $P_{\text{th}}$  or the smaller SNR will result in more weak MPCs to be detected, whereas it has a slight impact on the clustering results considering outlier detection and pruning procedures in the further developed multipath clustering algorithm.

The cluster nature of mmWave multipath channels indicates that clustering MPCs into several groups is a natural choice to investigate the impact of physical objects on mmWave propagation and exploit low-complexity low-power-consumption transceiver structures with respect to cluster-level space-time characteristics. The improvements in auto-clustering algorithms require that mmWave propagation characteristics in different environments be taken into account and that a reasonable similarity measure be used to quantify the distance between any two individual MPCs with clear physical explanation (He et al., 2018).

The widely used MPC distance (MCD) provides a distance measure of two MPCs in both delay and angular domains. Here, the MCD between the  $i^{\text{th}}$  and  $j^{\text{th}}$  MPCs (Czink et al., 2006b) in terms of our single-directional channel measurements is defined as

$$\text{MCD}_{ij} = \sqrt{\text{MCD}_{\Phi_{ij}}^2 + \text{MCD}_{\tau_{ij}}^2}, \quad (3)$$

where  $i, j \in \{1, 2, \dots, L\}$ ,  $i \neq j$ , with  $L$  being the number of estimated MPCs. The angular MCD of arrival is computed as

$$\text{MCD}_{\Phi_{ij}} = \frac{1}{2} \|\Phi_i - \Phi_j\|_2 \quad (4)$$

with  $\Phi = (\sin \theta \cos \phi, \sin \theta \sin \phi, \cos \theta)^T$ . The delay MCD is computed as

$$\text{MCD}_{\tau_{ij}} = \xi \frac{|\tau_i - \tau_j|}{\Delta \tau_{\max}} \frac{\tau_{\text{std}}}{\Delta \tau_{\max}} \quad (5)$$

with  $\xi$  being the delay scaling factor,  $\Delta \tau_{\max}$  the maximum delay difference over all pairs of MPCs, and

$\tau_{\text{std}}$  the standard deviation of delay. However, the delay differences among the finite detectable clusters in outdoor rich scattering environments are up to hundreds of nanoseconds (e.g., as shown in Fig. 4, where cluster 2 has an approximate 363.33 ns excess delay compared with cluster 1), leading to an imprecise measure of  $\Delta\tau_{\text{max}}$  and  $\tau_{\text{std}}$  when clustering compact MPCs in the time domain.

Hence, an improved auto-clustering algorithm is proposed to cluster MPCs twice, and for each step, the KPowerMeans clustering technique is used, which takes the MPC power into consideration (Czink et al., 2006a). The KPowerMeans algorithm assigns each MPC to the closest cluster centroid, and updates all the cluster centroids until they no longer change compared with the last iteration. The cluster centroid is defined as an MPC, which has a power-weighted mean of minimum sum of the distance to other MPCs within a cluster. During the clustering, the first step is mainly to distinguish all MPCs in the delay domain, usually using a large default value of  $\xi = 10$ ; the second step is mainly to group the MPCs in the angular domain, within each subset using the delay scaling factor  $\xi$  computed as (Ling et al., 2018)

$$\xi = \frac{\sqrt{\sum_{i=1}^{L_n} \sum_{j=1}^{L_n} \text{MCD}_{\tau_{ij}}^2}}{\sum_{i=1}^{L_n} \sum_{j=1}^{L_n} \left( \frac{|\tau_i - \tau_j|}{\Delta\tau_{\text{max}}} \frac{\tau_{\text{std}}}{\Delta\tau_{\text{max}}} \right)}, \quad (6)$$

where  $L_n$  is the number of MPCs in the  $n^{\text{th}}$  subset satisfying  $\sum_{n=1}^N L_n = L$ . The improved clustering algorithm first clusters the whole MPC set into several small data sets, while a more precise measure of delay MCD in Eq. (5) is performed for each small data set in the second-step clustering.

In addition, the KPowerMeans algorithm requires to specify a range for the expected number of clusters  $N$  and select initial cluster centroids as inputs. It is worth mentioning that the convergence speed of the clustering algorithm depends mostly on the initial centroid selection, whereby the nearer the initial centroid positions approximate to the final clustering results, the fewer iterations are likely to be required. We thus consider a dissimilarity matrix  $\mathbf{S} = (s_{ij})_{L \times L}$  with  $s_{ij}$  given by

$$s_{ij} = \frac{p_i + p_j}{2P_{\text{max}}} \text{MCD}_{ij}, \quad (7)$$

where  $p_i$  and  $p_j$  denote the power of the  $i^{\text{th}}$  and  $j^{\text{th}}$  MPCs, respectively.

When a pair of MPCs has as large path power and MCD as possible, corresponding to the increment of  $s_{ij}$ , these two MPCs can be selected as initial cluster centroids. After clustering  $L$  MPCs into the final  $K$  clusters, where  $K$  is usually larger than  $N$  due to the second-step clustering, it is necessary to detect and prune outliers. Here, two kinds of outliers are defined. First, for the cluster with few weak MPCs, we suppose that these MPCs do not belong to any cluster and should be removed directly. Second, some MPCs may stand out from a cluster due to unpredictable channel changing, so an eccentricity  $\Delta_i$  is used to measure how outliers stand out from the cluster centroid, expressed as

$$\Delta_i = \frac{\text{MCD}_{i,g_k}}{\frac{1}{L_k} \sum_{j=1}^{L_k} \text{MCD}_{j,g_k}}, \quad (8)$$

where  $g_k$  is the index of the cluster centroid in the  $k^{\text{th}}$  cluster with  $L_k$  MPCs in total. If  $\Delta_i$  is larger than the threshold  $\Delta_{\text{th}}$ , the  $i^{\text{th}}$  MPC is considered as an outlier and is pruned away. The unitless value of  $\Delta_{\text{th}}$  is determined by the rule that 99.7% of the values of  $\Delta_i$  are within three times standard deviations. To find the optimal number of clusters  $K$ , several cluster validation methods can be used, rather than visual inspection based on unpruned clusters (Sangodoyin et al., 2016). We thus apply the Silhouette index to determine the final clustering results with the maximum validation factor (Zhang et al., 2017).

Fig. 5 depicts an example of synthesized power delay angular profile (PDAP) calculated based on 180 measured CIRs for CBD-RX 38 at 28 GHz when the RX antenna is rotated in azimuth and elevation, as well as the MPC estimation and clustering results. It can be observed from Fig. 5a that the received signal energy concentrates mainly on a limited number of space-time blocks, corresponding to different propagation paths and mechanisms. Fig. 5b depicts the 360 estimated MPCs using the peak detection method with the power threshold of  $-76.4$  dBm as illustrated in Fig. 4. Following the proposed clustering algorithm, seven clusters are extracted (Fig. 5c), where the spots with the same color represent the subpaths in a cluster. Visual inspection shows that the result is reasonable and acceptable since the clusters are separated in delay and angular domains, and after pruning outliers, intra-cluster rays are compact to each cluster centroid. In combination with the layout-related analysis, cluster C1 corresponds

to the single-reflection from the metal billboard on the right side of RX 38. Clusters C2 and C3 correspond to double-reflection from the nearby and far LED screens on the left side, respectively, exhibiting approximately  $180^\circ$  AoA differences in comparison with cluster C1. Cluster C4 corresponds to the double-reflection (first by the LED screen and then by the external wall of the front building) which experiences longer propagation distance compared with the single-bounce cluster C1 but has larger path power. To the best of our understanding, this is because the AoAs of these two clusters are totally different, corresponding to different scatterers in realistic environments (the MPCs in cluster C4 are generally from the orientation of the main lobe of TX antenna pattern, while those in cluster C1 are from the side lobe). Clusters C5 and C6 are assumed to be high-order reflection of cluster C4. Apart from these dominant clusters, a weak cluster with large time delay (e.g., cluster C7) is detected, corresponding

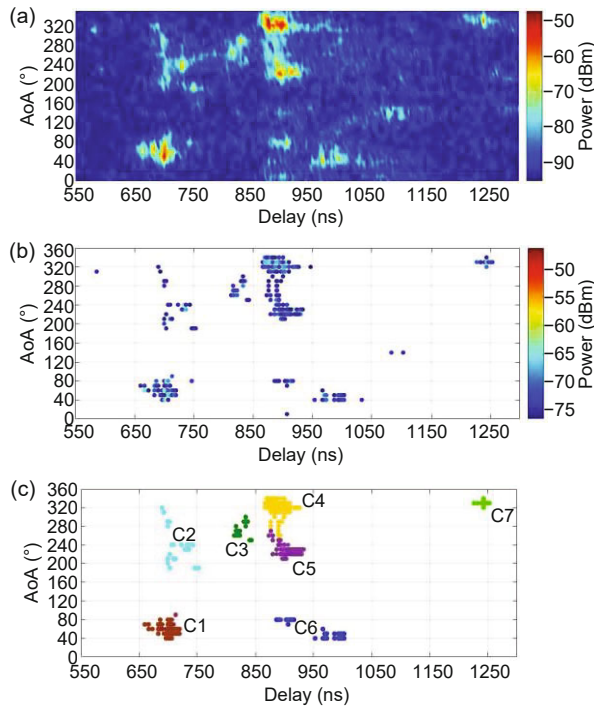


**Fig. 5** Synthesized 28 GHz power delay angular profile (PDAP) for RX 38 in the CBD-NLoS scenario with five elevation levels, and the multipath clustering results based on estimated MPCs: (a) PDAP calculated from the total 180 CIRs with different  $(\phi, \theta)$ ; (b) estimated effective MPCs using the peak detection algorithm; (c) clustering result using the improved KPowerMeans algorithm (References to color refer to the online version of this figure)

to more complicated propagation paths. Meanwhile, note that it becomes more accurate to distinguish different clusters, as well as their birth-death properties, if narrow-beam horn antennas with high gain are employed at the TX side.

Another set of measurement and clustering results in the DRA-NLoS scenario is depicted in Fig. 6, following the same measurement configurations and analysis methods as above, where a total of 565 MPCs and eight clusters are estimated with the detection level of  $-69.23$  dBm. To study mmWave propagation in detail, clusters corresponding to the surrounding scatterers are identified. Clusters C1, C2, C4, and C6 correspond to reflection from the exterior wall of a five-story building at the back of RX 29, and cluster C3 corresponds to diffraction over the rooftop of a six-story building in front of RX 29. Cluster C5 corresponds to the second-order reflected cluster from the front building. Cluster C7 is assumed to be a reflection of cluster C8 through the

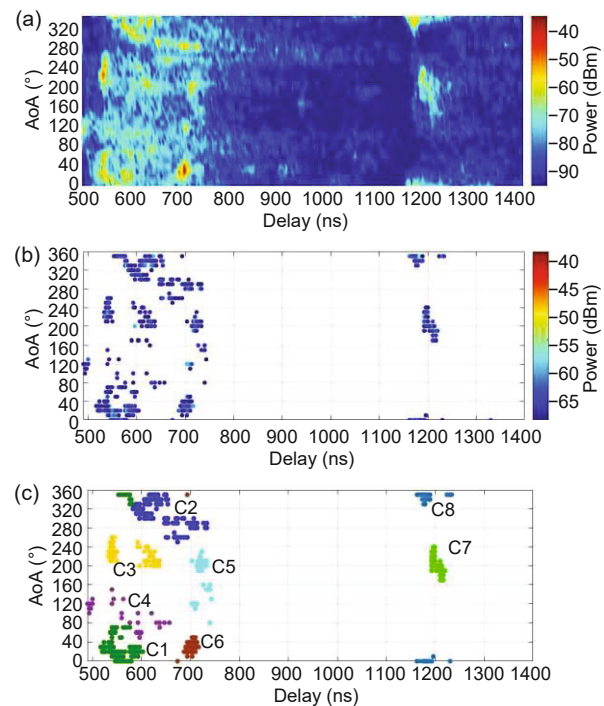


**Fig. 6** Synthesized 28 GHz power delay angular profile (PDAP) for RX 29 in the DRA-NLoS scenario with five elevation levels, and the multipath clustering results based on estimated MPCs: (a) PDAP calculated from the total 180 CIRs with different  $(\phi, \theta)$ ; (b) estimated effective MPCs using the peak detection algorithm; (c) clustering result using the improved KPowerMeans algorithm (References to color refer to the online version of this figure)

wall of the building behind RX 29. They have long delays with about 150 m extra propagation distance compared with most of the clusters. As illustrated in Figs. 5 and 6, reflection from the building exterior walls and diffraction over the building rooftop levels play a role in coverage enhancement of mmWave systems in UMa NLoS scenarios. Moreover, totally different space-time propagation characteristics can be observed, where the sparse nature of mmWave propagation is visible in the CBD environment with several well-separated clusters, but the clusters in the DRA environment are visually close to each other with probably larger intra-cluster angular spread.

Based on the clustered MPCs for tens of TX-RX combinations in all scenarios, inter- and intra-cluster properties of 28 and 39 GHz propagation channels are analyzed separately.

### 3.2 Composite and inter-cluster channel characteristics

Table 3 shows the statistics of composite and inter-cluster channel parameters, including composite delay and angular dispersions, Ricean  $K$ -factor,

and the number of clusters  $C$ . It can be observed that the mean of  $C$  decreases with the increment of carrier frequency due to fewer detectable clusters at higher frequency bands. In the CBD environment, the value of  $C$  for the NLoS link is significantly smaller than that for the LoS link, while there is a slight difference in the DRA environment. Moreover, rich scatterers exist in the CBD-LoS scenario, resulting in larger  $C$  compared with that in the DRA-LoS scenario. Unlike the measurement results in this study, the mean of  $C$  was 4.58 for the 28 GHz urban NLoS channel reported earlier (Ko et al., 2017), where the DSS method was also used to synthesize omnidirectional channel. The observations in the three dense urban environments indicate that the statistics of  $C$  is closely related to the concerned propagation scenarios and environments. It is also worth noting that the means of  $C$  extracted based on field measured data are significantly smaller than the default values in 3GPP mmWave channel models (3GPP, 2018), which are substituted by the simulation or measurement results below 6 GHz. Hence, the channel sparsity in the beamspace domain at mmWave

**Table 3 Statistics of inter- and intra-cluster channel parameters for UMa scenarios at 28 and 39 GHz bands**

Scenario	Composite DS <sup>+</sup> (lg(s))		Composite ASA* (lg(°))		Composite ZSA* (lg(°))		Ricean $K$ -factor	
	$\mu$	$\sigma$	$\mu$	$\sigma$	$\mu$	$\sigma$	$\mu$	$\sigma$
UMa, CBD, 28 GHz LoS	-6.73	0.26	1.84	0.20	0.90	0.13	7.34	2.68
UMa, CBD, 28 GHz NLoS	-7.00	0.23	1.76	0.30	0.87	0.09	NA	NA
UMa, CBD, 39 GHz LoS	-6.81	0.33	1.77	0.30	0.83	0.19	6.27	2.28
UMa, CBD, 39 GHz NLoS	-7.28	0.23	1.71	0.33	0.85	0.20	NA	NA
UMa, DRA, 28 GHz LoS	-7.02	0.23	1.79	0.21	1.00	0.15	7.71	1.07
UMa, DRA, 28 GHz NLoS	-6.79	0.29	1.87	0.29	0.97	0.11	NA	NA
UMa, DRA, 39 GHz LoS	-7.08	0.29	1.62	0.44	1.00	0.19	6.37	2.02
UMa, DRA, 39 GHz NLoS	-6.88	0.33	1.88	0.38	0.95	0.11	NA	NA

Scenario	Cluster No.		Cluster DS (ns)		Cluster ASA (°)		Cluster ZSA (°)	
	$\mu$	$\sigma$	$\mu$	$\sigma$	$\mu$	$\sigma$	$\mu$	$\sigma$
UMa, CBD, 28 GHz LoS	7.28	2.46	72.13	41.16	14.48	10.40	7.29	3.14
UMa, CBD, 28 GHz NLoS	5.92	1.89	37.37	31.10	10.12	6.82	6.56	2.22
UMa, CBD, 39 GHz LoS	7.13	3.03	62.81	46.26	12.66	11.21	7.03	2.96
UMa, CBD, 39 GHz NLoS	5.78	2.16	28.30	29.95	8.16	6.59	8.05	2.63
UMa, DRA, 28 GHz LoS	6.08	1.98	27.00	23.59	13.95	9.15	9.98	3.90
UMa, DRA, 28 GHz NLoS	6.30	3.36	30.56	27.97	14.24	11.79	7.50	3.18
UMa, DRA, 39 GHz LoS	5.42	2.68	21.09	24.99	11.17	10.23	7.90	4.11
UMa, DRA, 39 GHz NLoS	5.42	2.26	23.09	23.03	13.93	12.51	7.09	2.83

UMa: urban macrocell; CBD: central business district; DRA: dense residential area; LoS: line-of-sight; NLoS: non-line-of-sight; DS: delay spread; ASA: azimuth angular spread of arrival; ZSA: zenith angular spread of arrival; NA: not available. The upper part shows the composite channel parameters (Zhang et al., 2019), and the lower part shows the cluster-level channel parameters. <sup>+</sup>: The threshold of 8 dB above the noise floor is used for effective PDPs estimation (Wang et al., 2019) and RMS composite delay spread calculation (Rappaport et al., 2015). <sup>\*</sup>: The threshold of 25 dB below the peak level of the power angular profile is used for RMS angular spread calculation (ITU, 2017)

bands should be rather obvious compared with traditional microwave band. With the utilization of large antenna arrays, finite independent clusters indicate that the low-rank property of mmWave multiple-input multiple-output (MIMO) channels should be taken into account.

In the case of the LoS condition, the Ricean  $K$ -factor is considered as a large-scale channel parameter to scale the power ratio of the dominant MPC (typically the LoS component) to the remaining MPCs (3GPP, 2018; Huang et al., 2019). The  $K$ -factor is expressed as

$$K = \frac{V_D^2}{2\sigma^2}, \quad (9)$$

where  $V_D$  is the amplitude of the main CIR peak (i.e., the LoS component) and  $\sigma^2$  is the variance of amplitude representing the intensity of the fluctuating part (i.e., the multipath signals). When the  $K$ -factor tends to 0, the channel is dominated by NLoS paths reflected or diffracted from independent physical objects and the channel matrix probably has a large number of singular values. When it tends to infinity, the LoS component is dominant for the radio channel with low-rank property. The measured  $K$ -factors in CBD and DRA environments are modeled using lognormal distribution, and the goodness of the fit is evaluated by Kolmogorov-Smirnov (K-S) test at 5% significance level. Their statistics are presented in Table 3. It can be seen that the CBD-LoS link has a smaller Ricean  $K$ -factor due to existing rich NLoS MPCs, in comparison with the DRA-LoS link at 28 and 39 GHz. The result is consistent with the observations of composite delay and angular spreads reported by Zhang et al. (2019), where a larger  $K$ -factor likely leads to fewer detectable MPCs apart from the LoS path, corresponding to smaller composite DS and ASA. Fig. 7 depicts the cross-correlation coefficients of the Ricean  $K$ -factor, composite DS, ASA, and ZSA, where correlation coefficients between the Ricean  $K$ -factor and root-mean-squared (RMS) dispersion of parameters are generally smaller than zero at 28 GHz for negative correlation, and are within  $[-0.2, 0.2]$  at 39 GHz for less correlation. In addition, positive correlations among composite DS, ASA, and ZSA can be obtained for predicting temporal and angular channel characteristics and improving the reliability of mmWave communication systems.

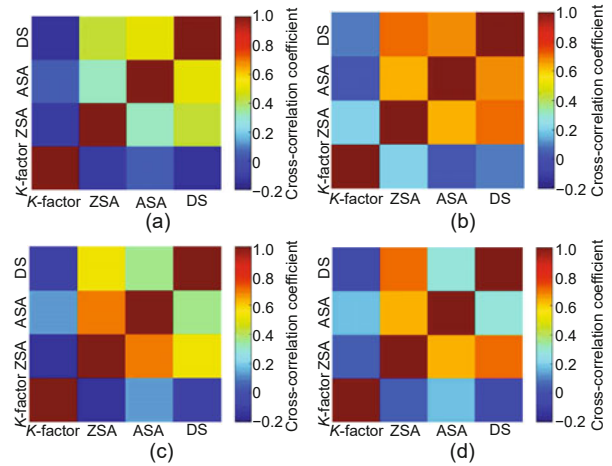


**Fig. 7** Cross-correlation coefficients of Ricean  $K$ -factor, composite delay spread, and composite angular spread in the LoS scenarios: (a) CBD at 28 GHz band; (b) CBD at 39 GHz band; (c) DRA at 28 GHz band; (d) DRA at 39 GHz band (References to color refer to the online version of this figure)

### 3.3 Intra-cluster delay and angular spreads

The cluster-level RMS DS is calculated following the similar definition in Rappaport et al. (2015). The statistics of cluster-based DS (including mean value  $\mu$  and standard deviation  $\sigma$ ) across different scenarios and frequencies are presented in Table 3. For LoS scenarios, the average intra-cluster DS at 28 and 39 GHz in CBD is 72.13 and 62.81 ns, respectively, and in DRA is 27.00 and 21.09 ns, respectively. This trend with regard to carrier frequency, as expected, depends on the difference in space-time propagation characteristics. Moreover, the mean values of cluster DS in DRA are significantly smaller than those in CBD under identical measurement setup. We speculate that this is because multiple reflections exist in CBD-like rich scattering environment. Note that the CBD-LoS scenario has a relatively large value of  $\sigma$  at both 28 and 39 GHz, compared with the DRA-LoS scenario. This phenomenon is due to the fact that propagation along continuous routes with only one sector in operation (e.g., DRA-LoS RXs served by sector 1) manifests smaller  $\sigma$ , whereas for the CBD-LoS scenario, RXs can be divided into two types (e.g., RX 1–8 along street canyon and RX 9–25 along open square) served by different sectors.

Fig. 8 depicts the empirical cumulative distribution functions (CDFs) of intra-cluster DS in the CBD and DRA environments. It can be observed that cluster DS for NLoS links is obviously smaller than

that for LoS links in the CBD environment, while an opposite result can be observed in the DRA environment. A simple explanation for this observation is that more diffused distribution of reflectors can be seen around RXs in the CBD-LoS scenario, leading to significant cluster DS compared with the results in other scenarios. In Table 3, statistics of cluster-level DS obtained from our measurements and 3GPP model (3GPP, 2018) are compared. Intuitively, identical cluster DS across LoS and NLoS links is shown in the 3GPP model and it is generally smaller than the result derived from this work. Similar behaviors can be observed in comparison with the field measurement result reported by Ko et al. (2017); therein, mean of cluster DS is 12.86 ns for the NLoS link in street canyon at 28 GHz. These differences indicate that it is of great importance to consider the effect of propagation environments in the deployment of

outdoor mmWave cellular networks.

The parameters associated with the intra-cluster RMS ASA and ZSA across 28 and 39 GHz for all scenarios are also provided in Table 3. Fig. 9 shows the CDFs of field measured intra-cluster ASA in CBD and DRA environments. The main conclusions drawn from the observations of the statistics of cluster ASA are the following: (1) cluster-level ASAs are significantly smaller than composite channel parameters, which characterize channel properties of directional transmission in the angular domain; (2) an increase in carrier frequency in general reduces the RMS cluster ASA for all scenarios, while slight difference can be observed between 28 and 39 GHz; (3) a similar behavior across LoS and NLoS links is seen between two concerned UMA environments, and this trend is consistent with the results of cluster DS as described before. Also, the

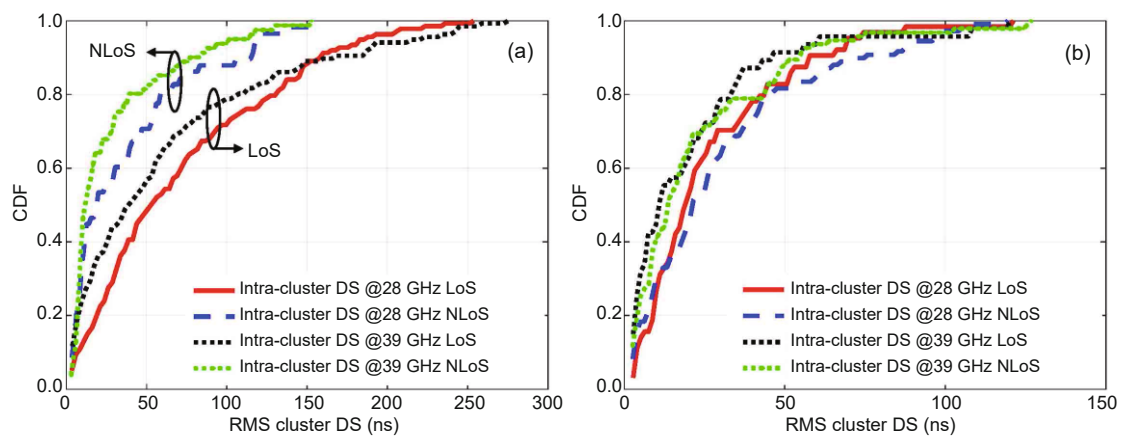


Fig. 8 Empirical cumulative distribution function (CDF) of cluster delay spread (DS) for LoS and NLoS scenarios across 28 and 39 GHz in CBD (a) and DRA (b) environments

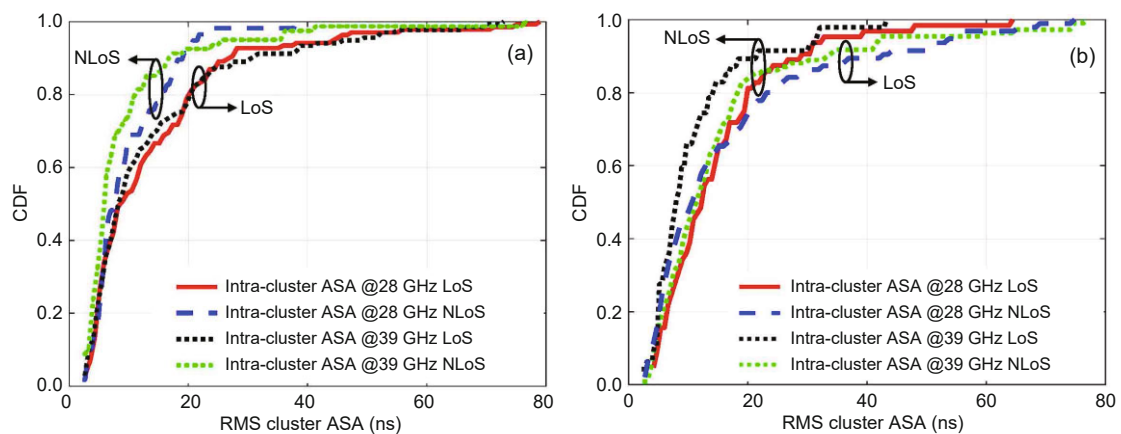
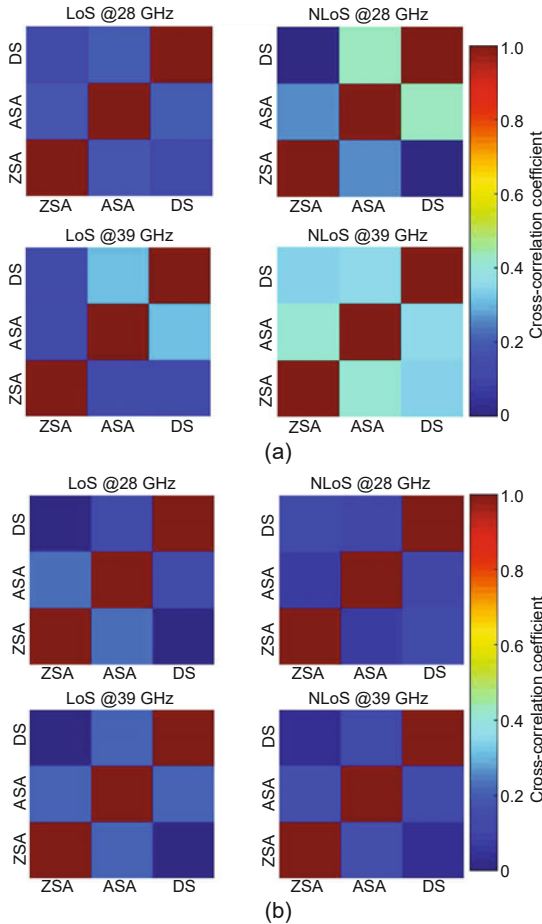


Fig. 9 Empirical cumulative distribution function (CDF) of cluster azimuth angular spread of arrival (ASA) for LoS and NLoS scenarios across 28 and 39 GHz in CBD (a) and DRA (b) environments

means of cluster ZSA are observed to be frequency-independent for all measured scenarios, and the maximum difference of  $2.1^\circ$  between composite and cluster-level RMS ZSA indicates that mmWave propagation in dense urban environments is more concentrated in elevation dimension within the vertical rotation range of  $[-20^\circ, 20^\circ]$  in our measurements. Hence, a low-complexity transmission scheme using two-dimensional (2D) beamforming is feasible in mmWave UMa downlink channels when TX antennas downtilt can be adjusted mechanically and RXs are within the same height.

### 3.4 Correlations of cluster-based channel parameters

Fig. 10 depicts the cross-correlation coefficients of cluster-level delay and angular spread across 28 and 39 GHz for both LoS and NLoS links using the



**Fig. 10** Cross-correlation coefficients of cluster-level delay and angular spread in CBD (a) and DRA (b) environments (References to color refer to the online version of this figure)

same colorbar for convenience. The cross-correlation coefficients among intra-cluster DS, ASA, and ZSA are generally within  $[0, 0.2]$  in LoS scenarios. Intuitively, this means that temporal and spatial propagation characteristics are less correlated or uncorrelated, with respect to the beamspace representation of outdoor mmWave channels in the presence of an LoS path. A similar behavior can be observed for the DRA-NLoS link, whereas the cross-correlation coefficients in CBD-NLoS are much larger. This phenomenon is consistent with the trend of intra-cluster parameters across LoS and NLoS links in CBD and DRA environments, due to the fact that well-separated clusters (e.g., as shown in Fig. 5 for the CBD-NLoS link) probably share similar intra-cluster distributions, in comparison to overlapped clusters (e.g., as shown in Fig. 6 for the DRA-NLoS link). Hence, the channel vectors are probably not independent and identically distributed in some specific scenarios at mmWave bands, a property that requires further understanding of the impact of actual physical scattering sources, corresponding to different propagation mechanisms, on the space-time variations of the properties of the clusters.

## 4 Analysis of propagation mechanisms and implications on system design

### 4.1 Reflection and diffraction

The cluster-level analysis of mmWave propagation characteristics for NLoS links in two dense urban environments shows that reflection and diffraction play a role in coverage enhancement of mmWave cellular networks. Existing site-specific channel measurements reveal that reflections become rich at mmWave band due to much smaller wavelength compared with the sizes of surrounding objects (Sato et al., 1997; Sun et al., 2018), whereas there is a dearth of outdoor field measurements to exploit their impacts on channel characterization. On the other hand, diffraction measurements show good fitness with the theoretical diffraction models in terms of modeling diffraction loss (Jacob et al., 2012; Kim et al., 2017; Rappaport et al., 2017). During the measurements, however, identical horn antennas with narrow HPBW are used at transceivers and always aimed at the diffraction points, rather than taking the impact of antenna radiation pattern into account

in real cellular-type channel modeling. Hence, to exploit the optimal transmission scheme for outdoor mmWave cellular system design, the impacts of reflection and diffraction on mmWave space-time propagation characteristics are investigated in two typical NLoS cases (Fig. 11). A diagram of the simplified NLoS case in CBD-like environments is shown in Fig. 11a, where the TX antenna locates on the rooftop with height  $h_1$ , and  $h_2$  denotes the height of a surrounding building which is close to  $h_1$ . Considering a downlink mmWave cellular network, mobile users in the shadow region can simultaneously receive diffraction signals over the building corners and reflection signals from the lit region when using wide-beam antennas at the TX side. Fig. 11b depicts a diagram of the other NLoS case in DRA-like environments, where the height of blockage  $h_2$  is much less than TX antenna height  $h_1$ . In general, RX in the shadow region can receive only diffracted signals over the rooftop, and for a special case, signals reflected from lit region can also be received to maintain a reliable link when RX is in deep-shadow regions with a large diffraction angle. The geometry-based analysis of dominant propagation mechanism reveals that most signals in the azimuth plane are blocked by the building corner and that signals in the elevation plane are blocked by the building rooftop, leading to huge differences in cluster-level spatial propagation characteristics.

Figs. 12a and 12b depict the distributions of received signals in the AoA domain varying with RX positions at 28 and 39 GHz in the CBD-NLoS scenario, where the number of most effective paths for each TX-RX pair is 30. Combined with the clustering results in the power-delay-angle domain (e.g., the original received data and clustering result shown in Fig. 5), MPCs with the highest power are concentrated within the angular range of  $[-60^\circ, 0^\circ]$ , corresponding to the second-order reflection (first by the LED screen on the bottom and then by the external wall of the front building). Meanwhile, remarkable AoA gaps between different reflected clusters indicate that reflection is closely related to the topologies of the deployment environments and serves as the dominant propagation mechanism to extend mmWave cell coverage in the CBD-like NLoS scenario. Figs. 12c and 12d show the measurement results at 28 and 39 GHz in the DRA environment, where the standard deviation of the AoA of the

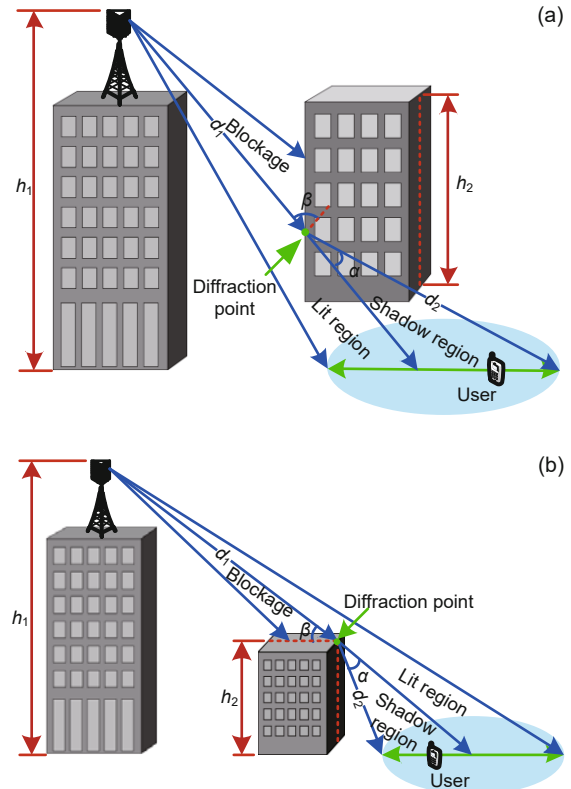


**Fig. 11 Illustration of propagation mechanisms in the CBD-like (a) and DRA-like (b) NLoS scenarios**

Blue lines: LoS paths; green lines: diffraction paths; red dots: diffraction points. References to color refer to the online version of this figure

strongest paths over 11 NLoS-RXs is significantly larger than that in the CBD environment. Moreover, it shows distinct differences between 28 and 39 GHz channels for DRA-RX 27–30, which are blocked by a six-story apartment. This is due to the fact that the rates of reflection and diffraction are fluctuant, where the diffraction over rooftop level is dominant at 28 GHz and the reflection from exterior walls is prominent at 39 GHz. This trend is in line with published diffraction measurement results (Jacob et al., 2012; Rappaport et al., 2017), showing that diffraction loss is proportional to the carrier frequency and that higher frequencies will cause larger loss at the same diffraction angle. For DRA-RX 25 and 32–35, only clusters formed by specular reflection can be extracted, indicating that extremely large fading needs to be overcome in deep shadow regions. The observations from Fig. 11 also confirm that cluster-level RMS ASA for the CBD-NLoS link is significantly smaller than that for the DRA-NLoS link (see Table 3), since most signals in the azimuth plane are

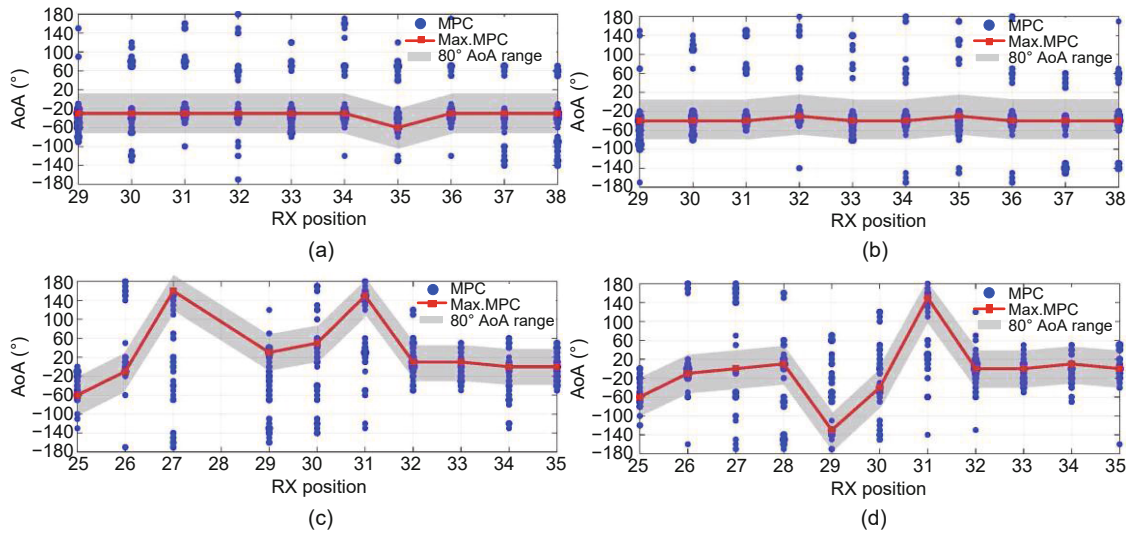


**Fig. 12** Distributions of 30 most effective multipath components (MPCs) for each TX-RX pair with respect to AoA in NLoS scenarios: (a) CBD, 28 GHz; (b) CBD, 39 GHz; (c) DRA, 28 GHz; (d) DRA, 39 GHz

Red squares represent MPCs having maximum received power among 30 MPCs and the size of blue dots represents the path power. References to color refer to the online version of this figure

blocked by building corners and split into several narrow beams, thus exploiting rich reflections from external walls of surrounding buildings.

#### 4.2 Implications on mmWave system design

Based on the cellular-type channel measurements in two typical dense urban environments at two priority 5G candidate mmWave bands, the cluster-based analysis of space-time channel characteristics is developed to the detailed level, focusing on the identification of the scattering sources for strong clusters in the sense of path power and the impact of corresponding propagation mechanisms. Hence, the following implications on outdoor mmWave macro-cellular system design can be observed:

1. The channel measurements presented in this work reveal that the reflection and diffraction from surrounding objects extend the coverage of mmWave cellular systems in UMa scenarios. They can provide only dramatically worse coverage with the radius up to 200 m for NLoS links; it is also necessary to use large-scale antenna arrays with sufficient gains at the TX side to mitigate the severe path loss above 6 GHz.

2. When comparing the Ricean  $K$ -factor across 28 and 39 GHz, the power of LoS signals decreases rapidly with increasing frequency. This observation indicates that single-cell cellular systems operating at 28 GHz are prior to be deployed in UMa scenar-

ios, because received signals at 39 GHz are relatively weak and even beyond the limit of RX sensitivity level. Thus, larger transmit power and more antenna elements are necessary for 39 GHz radio systems.

3. The clustering of multipath in delay and angular domains takes advantage of beamspace representation of mmWave channels to exploit directional transmission in 5G mmWave communications. The smaller number of clusters for higher frequencies in dense urban environments (e.g., 5–6 for LoS links and 6–7 for NLoS observed in this study), in comparison to traditional microwave bands (3GPP, 2018), indicates that the basic assumption of sparse property is reasonable for mmWave channels, and that the high spatial resolution claimed by massive MIMO technologies can be realized.

4. Cluster-level channel parameters are in general inversely proportional to the carrier frequency, albeit with an exception with regard to ZSA which is seen to be frequency-independent. A smaller angular spread at 39 GHz corresponds to narrower beamwidth along with the improvement of SNR and antenna gain. Moreover, diffraction frequently occurs with smaller propagation delay in residential environments at 28 GHz, whereas reflection becomes dominant with the increasing carrier frequency.

5. It must be pointed out that, in CBD-type environments, the centralized hybrid beamforming systems with finite RF chains are cost-efficient in

providing reliable links for users belonging to different well-separated clusters. Moreover, it is possible to acquire high-dimensional channel state information using low-rank channel estimation methods (Xie et al., 2016). By contrast, clusters in DRA-type environments overlap with each other and have broad ASA for NLoS links, bringing serious challenge to distinguish users totally in beamspace, making distributed antenna systems more suitable.

6. Based on the cluster-level channel characterization, the averages of intra-cluster RMS DS and ASA are significantly smaller than the composite results. As a consequence, the beamformer structure and beam scanning algorithm need to be carefully designed in both the initial access phase and data transmission phase, taking account of a tradeoff among efficiency, latency, and complexity (Li Q et al., 2015). On the other hand, considerable deviation exists in cluster temporal and azimuthal dispersion, which means that the adjustment of system configurations according to serving scenarios is necessary in outdoor mmWave cellular network deployment.

7. In the elevation dimension, ZoAs concentrate mainly in a small space when height difference between TX and RX antennas is more than 40 m, corresponding to small composite and cluster ZSA. Thus, 2D beamforming scheme is feasible for outdoor downlink transmission with a fixed antenna downtilt, while 3D beamforming scheme probably enables coverage extension for an outdoor-to-indoor scenario when users are located on different floors with different heights.

## 5 Conclusions

Full knowledge of propagation characteristics is the basis of cost-efficient design and deployment of future outdoor mmWave communication systems. In this work, cluster-based characterization of outdoor mmWave channels in two UMa scenarios has been developed based on extensive directional channel sounding data and the improved KPowerMeans multipath clustering algorithm.

From the clustering results, a finite number of strong clusters (e.g., 5–7) would be enough to describe mmWave multipath channels for UMa LoS/NLoS links. Measured composite and intra-cluster parameters, such as RMS DS and ASA, are all monotonic with frequency, whereas ZSAs are ob-

served to be frequency-independent. A comparison of channel characteristics across LoS and NLoS scenarios shows that in the CBD environment, the statistics of temporal and azimuthal dispersion in the LoS condition are much larger than those in the NLoS condition, while an opposite behavior can be observed in the DRA environment. Furthermore, the mapping results between detected clusters and physical objects indicate that reflection and diffraction are dominant for coverage enhancement when direct paths are blocked by surrounding buildings. The theoretical analysis of the KED model shows that diffraction over the rooftop level probably results in a larger ASA compared with diffraction over the building corner when using wide-beam antennas at the TX side, which provides a reasonable explanation for previous observations in NLoS scenarios. The cluster-level channel characteristics obtained in this study are more realistic in describing mmWave channels in dense urban environments.

## Contributors

Haiming WANG, Wei HONG, and Peize ZHANG designed the research. Peize ZHANG processed the data and drafted the manuscript. Haiming WANG and Peize ZHANG revised and finalized the paper.

## Compliance with ethics guidelines

Peize ZHANG, Haiming WANG, and Wei HONG declare that they have no conflict of interest.

## References

- 3GPP, 2018. Study on Channel Model for Frequency from 0.5 to 100 GHz. 3GPP TR 38.901 (V15.0.0).
- Andrews JG, Bai TY, Kulkarni MN, et al., 2017. Modeling and analyzing millimeter wave cellular systems. *IEEE Trans Commun*, 65(1):403-430. <https://doi.org/10.1109/TCOMM.2016.2618794>
- Bai TY, Alkhateeb A, Heath RW, 2014. Coverage and capacity of millimeter-wave cellular networks. *IEEE Commun Mag*, 52(9):70-77. <https://doi.org/10.1109/MCOM.2014.6894455>
- Bas CU, Kristem V, Wang R, et al., 2019. Real-time ultra-wideband channel sounder design for 3–18 GHz. *IEEE Trans Commun*, 67(4):2995-3008. <https://doi.org/10.1109/TCOMM.2018.2889487>
- Czink N, Cera P, Salo J, et al., 2006a. A framework for automatic clustering of parametric MIMO channel data including path powers. Proc IEEE Vehicular Technology Conf, p.1-5.
- Czink N, Cera P, Salo J, et al., 2006b. Improving clustering performance using multipath component distance. *Electron Lett*, 42(1):33-35. <https://doi.org/10.1049/el:20063917>

- Dupleich D, Müller R, Skoblikov S, et al., 2019. Multi-band double-directional 5G street canyon measurements in Germany. *Proc European Conf on Networks and Communications*, p.123-127.  
<https://doi.org/10.1109/EuCNC.2019.8801951>
- Haneda K, Omaki N, Imai T, et al., 2016. Frequency-agile pathloss models for urban street canyons. *IEEE Trans Antenn Propag*, 64(5):1941-1951.  
<https://doi.org/10.1109/TAP.2016.2536170>
- He RS, Ai B, Molisch AF, et al., 2018. Clustering enabled wireless channel modeling using big data algorithms. *IEEE Commun Mag*, 56(5):177-183.  
<https://doi.org/10.1109/MCOM.2018.1700701>
- Huang C, Molisch AF, Wang R, et al., 2019. Angular information-based NLOS/LOS identification for vehicle to vehicle MIMO system. *Proc IEEE Int Conf on Communications Workshops*, p.1-6.  
<https://doi.org/10.1109/ICCW.2019.8756726>
- Hur S, Baek S, Kim B, et al., 2016. Proposal on millimeter-wave channel modeling for 5G cellular system. *IEEE J Sel Top Signal Process*, 10(3):454-469.  
<https://doi.org/10.1109/JSTSP.2016.2527364>
- ITU, 2017. Multipath Propagation and Parameterization of Its Characteristics. ITU-R P.1407-6.
- ITU, 2019. ITU World Radiocommunication Conference Agrees Key Parameters for Future Communication Technologies.  
<https://www.itu.int/en/mediacentre/Pages/2019-PR24.aspx> [Accessed on Sept. 8, 2020].
- Jacob M, Priebe S, Dickhoff R, et al., 2012. Diffraction in mm and sub-mm wave indoor propagation channels. *IEEE Trans Microw Theory Techn*, 60(3):833-844.  
<https://doi.org/10.1109/TMTT.2011.2178859>
- Kim KW, Kim MD, Park JJ, et al., 2017. Diffraction loss model based on 28 GHz over-rooftop propagation measurements. *Proc IEEE 86<sup>th</sup> Vehicular Technology Conf*, p.1-5.  
<https://doi.org/10.1109/VTCFall.2017.8287881>
- Ko J, Cho YJ, Hur S, et al., 2017. Millimeter-wave channel measurements and analysis for statistical spatial channel model in in-building and urban environments at 28 GHz. *IEEE Trans Wirel Commun*, 16(9):5853-5868.  
<https://doi.org/10.1109/TWC.2017.2716924>
- Li J, Zhang PZ, Yu C, et al., 2019. High-efficiency wideband millimeter-wave channel sounder system. *Proc 13<sup>th</sup> European Conf on Antennas and Propagation*, p.1-5.
- Li Q, Shirani-Mehr H, Balercia T, et al., 2015. Millimeter wave channel model and system design considerations. *Proc IEEE Int Conf on Communication Workshop*, p.1214-1219.  
<https://doi.org/10.1109/ICCW.2015.7247343>
- Ling C, Yin XF, Müller R, et al., 2018. Double-directional dual-polarimetric cluster-based characterization of 70–77 GHz indoor channels. *IEEE Trans Antenn Propag*, 66(2):857-870.  
<https://doi.org/10.1109/TAP.2017.2772019>
- MacCartney GR, Rappaport TS, 2017. A flexible millimeter-wave channel sounder with absolute timing. *IEEE J Sel Areas Commun*, 35(6):1402-1418.  
<https://doi.org/10.1109/JSAC.2017.2687838>
- Raghavan V, Partyka A, Akhoondzadeh-Asl L, et al., 2017. Millimeter wave channel measurements and implications for PHY layer design. *IEEE Trans Antenn Propag*, 65(12):6521-6533.  
<https://doi.org/10.1109/TAP.2017.2758198>
- Rappaport TS, Deng SJ, 2015. 73 GHz wideband millimeter-wave foliage and ground reflection measurements and models. *Proc IEEE Int Conf on Communication Workshop*, p.1238-1243.  
<https://doi.org/10.1109/ICCW.2015.7247347>
- Rappaport TS, Ben-Dor E, Murdock JN, et al., 2012. 38 GHz and 60 GHz angle-dependent propagation for cellular & peer-to-peer wireless communications. *Proc IEEE Int Conf on Communication*, p.4568-4573.  
<https://doi.org/10.1109/ICC.2012.6363891>
- Rappaport TS, Sun S, Mayzus R, et al., 2013. Millimeter wave mobile communications for 5G cellular: it will work! *IEEE Access*, 1:335-349.  
<https://doi.org/10.1109/ACCESS.2013.2260813>
- Rappaport TS, MacCartney GR, Samimi MK, et al., 2015. Wideband millimeter-wave propagation measurements and channel models for future wireless communication system design. *IEEE Trans Commun*, 63(9):3029-3056.  
<https://doi.org/10.1109/TCOMM.2015.2434384>
- Rappaport TS, MacCartney GR, Sun S, et al., 2017. Small-scale, local area, and transitional millimeter wave propagation for 5G communications. *IEEE Trans Antenn Propag*, 65(12):6474-6490.  
<https://doi.org/10.1109/TAP.2017.2734159>
- Roh W, Seol JY, Park J, et al., 2014. Millimeter-wave beamforming as an enabling technology for 5G cellular communications: theoretical feasibility and prototype results. *IEEE Commun Mag*, 52(2):106-113.  
<https://doi.org/10.1109/MCOM.2014.6736750>
- Saad W, Bennis M, Chen MZ, 2020. A vision of 6G wireless systems: applications, trends, technologies, and open research problems. *IEEE Netw*, 34(3):134-142.  
<https://doi.org/10.1109/MNET.001.1900287>
- Samimi MK, Rappaport TS, 2016. 3-D millimeter-wave statistical channel model for 5G wireless system design. *IEEE Trans Microw Theory Techn*, 64(7):2207-2225.  
<https://doi.org/10.1109/TMTT.2016.2574851>
- Sangodoyin S, Kristem V, Molisch AF, et al., 2016. Statistical modeling of ultrawideband MIMO propagation channel in a warehouse environment. *IEEE Trans Antenn Propag*, 64(9):4049-4063.  
<https://doi.org/10.1109/TAP.2016.2583477>
- Sato K, Manabe T, Ihara T, et al., 1997. Measurements of reflection and transmission characteristics of interior structures of office building in the 60-GHz band. *IEEE Trans Antenn Propag*, 45(12):1783-1792.  
<https://doi.org/10.1109/8.650196>
- Sohrabi F, Yu W, 2016. Hybrid digital and analog beamforming design for large-scale antenna arrays. *IEEE J Sel Top Signal Process*, 10(3):501-513.  
<https://doi.org/10.1109/JSTSP.2016.2520912>
- Sun RY, Gentile CA, Senic J, et al., 2018. Millimeter-wave radio channels vs. synthetic beamwidth. *IEEE Commun Mag*, 56(12):53-59.  
<https://doi.org/10.1109/MCOM.2018.1800177>
- Wang HM, Gao XQ, Jiang B, et al., 2007. Efficient MIMO channel estimation using complementary sequences. *IET Commun*, 1(5):962-969.  
<https://doi.org/10.1049/iet-com:20060581>

- Wang HM, Zhang PZ, Li J, et al., 2019. Radio propagation and wireless coverage of LSAA-based 5G millimeter-wave mobile communication systems. *China Commun*, 16(5):1-18. <https://doi.org/10.23919/j.cc.2019.05.001>
- Xiao M, Mumtaz S, Huang YM, et al., 2017. Millimeter wave communications for future mobile networks. *IEEE J Sel Areas Commun*, 35(9):1909-1935. <https://doi.org/10.1109/JSAC.2017.2719924>
- Xie HX, Gao FF, Jin S, 2016. An overview of low-rank channel estimation for massive MIMO systems. *IEEE Access*, 4:7313-7321. <https://doi.org/10.1109/ACCESS.2016.2623772>
- You XH, Wang CX, Huang J, et al., 2021. Towards 6G wireless communication networks: vision, enabling technologies, and new paradigm shifts. *Sci China Inform Sci*, 64(1):110301. <https://doi.org/10.1007/s11432-020-2955-6>
- Yu XH, Zhang J, Haenggi M, et al., 2017. Coverage analysis for millimeter wave networks: the impact of directional antenna arrays. *IEEE J Sel Areas Commun*, 35(7):1498-1512. <https://doi.org/10.1109/JSAC.2017.2699098>
- Yuan YF, Zhao YJ, Zong BQ, et al., 2020. Potential key technologies for 6G mobile communications. *Sci China Inform Sci*, 63(8):183301. <https://doi.org/10.1007/s11432-019-2789-y>
- Zhang PZ, Wang HB, Zhou Y, et al., 2017. An improved three-dimensional auto-clustering algorithm for indoor millimeter-wave multipath propagation analysis. Proc IEEE/CIC Int Conf on Communications in China, p.1-6. <https://doi.org/10.1109/ICCChina.2017.8330409>
- Zhang PZ, Li J, Wang HB, et al., 2018. Indoor small-scale spatiotemporal propagation characteristics at multiple millimeter-wave bands. *IEEE Antenn Wirel Propag Lett*, 17(12):2250-2254. <https://doi.org/10.1109/LAWP.2018.2872051>
- Zhang PZ, Li J, Wang HM, et al., 2019. Millimeter-wave space-time propagation characteristics in urban macro-cell scenarios. Proc IEEE Int Conf on Communications, p.1-6. <https://doi.org/10.1109/ICC.2019.8761087>
- Zhao H, Mayzus R, Sun S, et al., 2013. 28 GHz millimeter wave cellular communication measurements for reflection and penetration loss in and around buildings in New York city. Proc IEEE Int Conf on Communications, p.5163-5167. <https://doi.org/10.1109/ICC.2013.6655403>